

In situ EBSD study of deformation behavior of primary α phase in a bimodal Ti-6Al-4V alloy during uniaxial tensile tests

Wansong Li*, Shigeto Yamasaki, Masatoshi Mitsuhashi, Hideharu Nakashima

Department of Advanced Materials Science and Engineering, Kyushu University, Fukuoka 8168580, Japan



ARTICLE INFO

Keywords:

Electron backscatter diffraction
Deformation
Grain rotation
Texture
Slip system
In situ tensile test

ABSTRACT

Uniaxial tension experiments and electron backscatter diffraction were performed on a bimodal Ti-6Al-4V alloy to study in situ the deformation behavior of primary hcp-Ti (α_p). It was found that the strain could be accommodated by the activation of slip systems and by grain rotations. The prismatic slip was the primary slip mode of the α_p . From the analysis of kernel average misorientation and geometrically necessary dislocation, it was shown that the dislocations mainly distributed in the vicinity of grain and sub-grain boundaries, and part of the dislocations distributed around slip lines. It was the dislocation activities that led to the formation of the low angle grain boundary and its transformation to the high angle grain boundary. It's important that tracking of deformation heterogeneities with significance to performance. By analyzing the rotation angle, average rotation rate, and rotation path of grains, it was shown that grain rotation heterogeneity occurred during the deformation. From the observation of the loading direction, grain rotation paths kept with the texture evolution direction of all α_p . The grains activated in the basal slip gradually rotated to the $\langle 10\bar{1}1 \rangle$ pole and enhanced the intensity of the $\langle 10\bar{1}1 \rangle$ texture. Meanwhile, the grains activated in prismatic or 1st-order pyramidal slip rotated to the $\langle 10\bar{1}0 \rangle$ pole and enhanced the intensity of the $\langle 10\bar{1}0 \rangle$ texture. Grain rotation and texture evolution are related to mechanical properties.

1. Introduction

Among the Ti alloys, Ti-6Al-4V possesses excellent mechanical properties/weight ratios and high corrosion resistance. These are most widely used in the aerospace industry [1–3]. A typical Ti-6Al-4V having a bimodal microstructure comprises an equiaxed primary hcp-Ti (α_p) and a lamellar secondary hcp-Ti (α_s)/bcc-Ti (β). Its deformation process mainly relies on the effect of α because of the low volume fraction of β [4]. α_p , the major constituent (> 50% in vol%) of all α , plays a significant role in resisting plastic deformation.

Many efforts have been made to investigate the deformation behavior of Ti alloys. Most studies have focused on the active slip modes of the dominant α phase and its dislocation slip and twinning in pure Ti [3,5–8]. Several studies have been devoted to the process of strain-induced twinning [7], slip transmissions [9,10], active slip systems [11], and the effect of strain rates [12,13] on Ti alloys having dual phases using a tension or compression experiment.

Understanding the influence of deformation heterogeneities on work hardening behavior can be useful to improving the deforming capabilities. Under plastic deformation, grain rotation can occur in various materials [14–17]. According to the investigation of

polycrystalline Al alloys, grain rotation occurs and is strongly affected by the initial orientation of each grain during deformation [18,19]. The rotation paths are approximately straight with lower strains, whereas some paths do not remain straight with high strain [18]. Owing to the difference in active slip systems, different rotation paths and rotation rates resulted among the different grains and within a single grain [20]. These effects of grain rotation behavior are expected to significantly influence the deformation behavior of α_p in Ti-6Al-4V [21]. Zhang et al. [11] found that the slip line in the α_p was the primary deformation mechanism of Ti-17 alloy with a bimodal microstructure during the tensile process. However, in that work, grain rotation behavior was not discussed in detail. However, the effect of the orientation and the neighboring grains on α_p grains were quantitatively analyzed by Ashish et al. [21] for polycrystalline Ti-6Al-4V. Unfortunately, the influence of the slip system and texture evolution on α_p was not considered.

From extant studies, the deformation mechanism of α_p in the bimodal Ti-6Al-4V alloy is still not completely understood. This is especially true, considering the grain rotation behavior of α_p . Thus, the present work investigates the deformation behavior of α_p in a bimodal Ti-6Al-4V alloy by using electron backscatter diffraction (EBSD) and in situ tensile tests, using the plane-trace method and inverse pole figure

* Corresponding author.

E-mail address: wqli0812@gmail.com (W. Li).

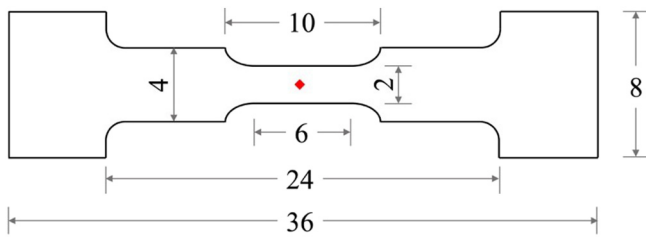


Fig. 1. Schematic of the specimen used for in situ tensile test and EBSD (dimensions are in mm).

(IPF) analysis, activated slip system, rotation angle, rotation rate, and rotation path of α_p . Additionally, the relationship between grain rotation path and texture evolution is analyzed.

2. Experimental

2.1. Materials

The studied material was an ingot of Ti-6.4Al-4.2V-0.2O-0.2Fe (at. %) alloy subjected to solution treatment at an inter-critical temperature of 940 °C for 2 h. It was subsequently water-cooled to room temperature followed by aging heat treatment at 705 °C for 3 h. It was then air-cooled to room temperature. All specimens were cut from the plate after heat treatment.

2.2. In situ tensile tests and EBSD measurements

The sample for the in situ tensile test was prepared via mechanical processing with a gauge length of 6 mm, a gauge width of 2 mm, and a thickness of 1 mm, as shown in Fig. 1. The to-be-tested area was marked using a small Vickers indentation at the center of the tensile specimen to act as a reference point for EBSD observation. Displacement-controlled tensile tests were then performed using a field emission scanning electron microscope (Ultra 55, Zeiss) equipped with a tensile tester. The extension rate of the in situ tensile test was $5 \times 10^{-4}/\text{s}$. The in situ tensile test was suspended (interrupted) when the displacement reached the given value.

The specimen for EBSD measurement was processed using the conventional technique. Afterward, it was polished using a colloidal silica suspension. EBSD measurements were performed at an accelerating voltage of 20 kV, a working distance of 20 mm, an aperture size of 120 μm , and a step size of 0.5 μm . The corresponding data were post-processed using OIM 7 software.

2.3. Regular tensile test

The specimen for the regular tensile test was cut into the same shape and tested under the same conditions with the sample for the in situ tensile analysis. However, the regular (continuous) tensile test was not suspended until it was broken off.

3. Results

3.1. Macroscopic strain–stress curves

Fig. 2 shows the macroscopic curves of tensile tests, in which black and gray correspond to in situ tensile and regular tensile tests, respectively. As seen in this figure, the in situ tensile test was interrupted six times for the EBSD experiment. The displacement of the sample has kept no change each time the in situ tensile tests suspended. Owing to stress relaxation, the curve of the in situ tensile shows six small loading drops (numbered 1–6). The corresponding strains and plastic strains for the six drops were measured when the in situ tensile tests suspended, as presented in Table 1. Table 2 lists the mechanical properties of the

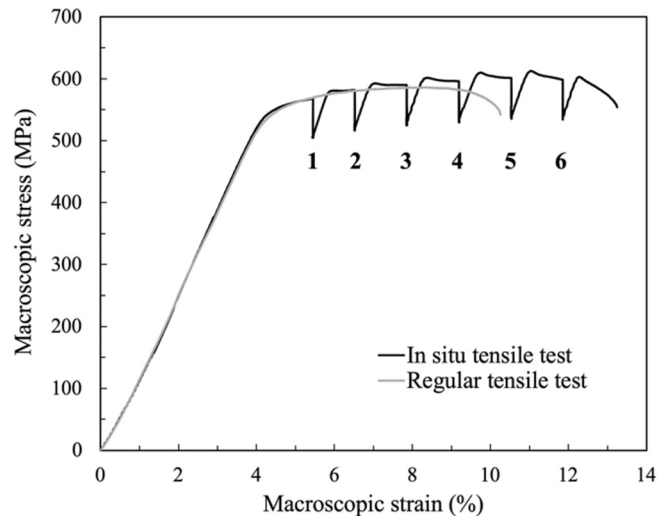


Fig. 2. Macroscopic stress–strain curves of the specimen recorded during in situ (black) and regular tensile tests (gray).

Table 1

Drops and corresponding strains and plastic strains obtained from the in situ tensile test for Ti-6Al-4V.

Drop	1	2	3	4	5	6
Strain (%)	5.5	6.5	7.9	9.2	10.5	11.9
Plastic strain (%)	1.2	2.2	3.6	4.9	6.2	7.6

specimen for the in situ and regular tensile tests. The measured stress of in situ tensile test happened when the test suspended. Table 2 indicates that there was almost no difference in the yield strength of the two samples obtained from the in situ and regular tensile tests. However, the measured tensile strength and elongation by the in situ tensile test was higher than those measured by the regular tensile test. Such a difference may be caused by creep behavior during the loading stops of the in situ tensile test [22].

3.2. Initial microstructure

Fig. 3(a) shows the secondary electron (SE) morphology observed prior to EBSD measurement without strain. This figure shows that the specimen had a typical bimodal structure comprising α_p and lamellar α_s/β , and it was used to distinguish α_p and α_s on the EBSD maps. Fig. 3(b) shows the IPF images of the microstructure corresponding to the same area in Fig. 3(a). Fig. 3(c), (d), and (e) show the IPF of β phase, the IPF of α_p , and that of α_s , respectively. Three axes of the specimens are defined in Fig. 3. Thus, the view direction of the figure reflects the normal direction (ND) of the plate specimen, the horizontal direction for the loading direction (LD), and the vertical direction for the transverse direction (TD). As presented in Fig. 3(c), the β phase is homogeneously distributed in the matrix and only takes up to 2.3% (vol.) of the microstructure. As observed in Fig. 3(d) and (e), the α_p and α_s can be distinguished from the IPF maps, owing to their different morphology features obtained from the SE image (Fig. 3(a)). The ratio of α_p is about 56.8% (vol.) of the microstructure.

3.3. Grain boundaries and dislocations

Fig. 4 displays the IPF maps and grain boundaries of α_p in the same area with different strains. In these maps, dark regions are the non- α_p positions, and the black and white lines reflect the high angle ($> 15^\circ$) grain boundary (HAGB) and low angle ($2\text{--}15^\circ$) grain boundary (LAGB), respectively. The deformation process of the grain boundary under strain can be characterized using typical grains, as marked by the red

Table 2

Mechanical properties of two Ti-6Al-4V specimens measured from in situ and regular tensile tests.

Specimen	Yield strength (MPa)	Tensile strength (MPa)	Uniform elongation (%)	Total elongation (%)
In situ	541	612	11.0	13.3
Regular	536	586	8.4	10.3

squares in Fig. 4. Red arrows in this figure index three positions (i.e., A1, A2, and A3) in one of these grains. At a plastic tension of 1.2% in Fig. 4(b), A2 transformed partly from LAGB into HAGB. The position of A1 and A3 had no transformation at the grain boundary. When the plastic strain increased to 2.2%, as shown in Fig. 4(c), A2 transformed further, and A1 underwent the change from LAGB into HAGB. With an increase in plastic strain to 3.6% (Fig. 4(d)), A1 and A2 transformed further, and their transformed HAGBs connected. Meanwhile, some short LAGBs appeared in A3. After the plastic strain reached 4.9%, as shown in Fig. 4(e), the connected HAGBs in A1 and A2 became sharp, and the formed LAGB in A3 extended in length.

Kernel average misorientation (KAM) and geometrically necessary dislocation (GND) are used to qualitatively analyze the dislocation density of the material [23–25]. Fig. 5(a)–(c) show KAM maps under different strains, and Fig. 5(d)–(f) show the corresponding GND maps, respectively. The KAM maps in Fig. 5(a)–(c) correspond to the same area in Fig. 4(a), (b), and (e), respectively. KAM values (degree) are divided into ranges and displayed as different colors, with blue showing the lowest KAM value (0–1°) and red showing the highest value (4–5°). The misorientations > 5° were excluded from the KAM value calculations. In the GND maps, different colors represent the different dislocation densities. The KAM maps show that the green and yellow areas of some grains increased continuously with the increasing strain,

indicating that the KAM values of these grains gradually increased. The GNDs also increased during the deformation; this the amplification of yellow and red area in GND maps can support. Furthermore, KAM values and GNDs presenting different variations within each grain, showing that the inhomogeneity of dislocation distribution occurred during the strain in individual grains. Compared with the IPF maps in Fig. 4, it can be seen that the increased KAM values and GNDs distributed primarily near grain and sub-grain boundaries in a preferentially distributed manner. Moreover, by comparing them with image quality (IQ) maps, it is evident from Fig. 5(b) that some green areas increased around slip lines, as marked by red arrows. That is to say, some dislocations partially concentrated around slip lines. The evolution of the KAM value and GNDs could be used to explain the formation process of LAGBs. During the deformation, the slip line formed in grains, and the dislocations glided, leading to a higher dislocation density near the slip line, grain boundaries, and sub-grain boundaries. Additionally, the dislocation tangle or wall forms in a position, such as B1, B2, or B3 (A3 in Fig. 4(e)) and would form the LGABs with a further strain [26,27]. Furthermore, as the strain increases, the local misorientation increases in the preferential position, which promotes the formation of LAGBs and its transformation from LAGBs to HAGBs. Besides, the dislocation gliding could lead to the sub-grain rotation, which also causes the transformation from LAGBs to HAGBs

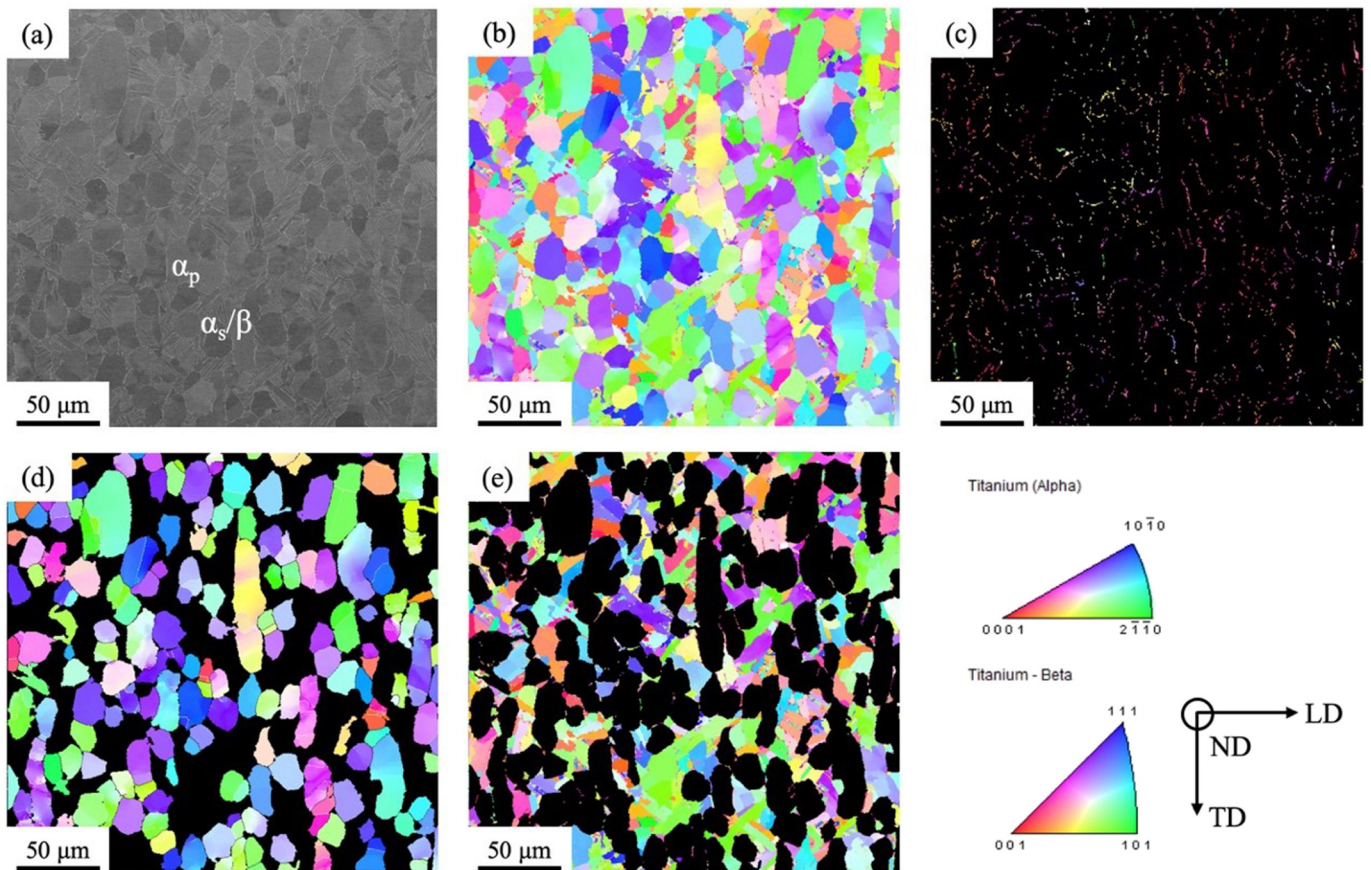


Fig. 3. Microstructures of the specimen for the same area with no strain: (a) SE morphology; (b) IPF of the specimen; (c) IPF of β phase; (d) IPF of α_p ; and (e) IPF of α_s . (ND: normal direction; TD: transverse direction; LD: loading direction).

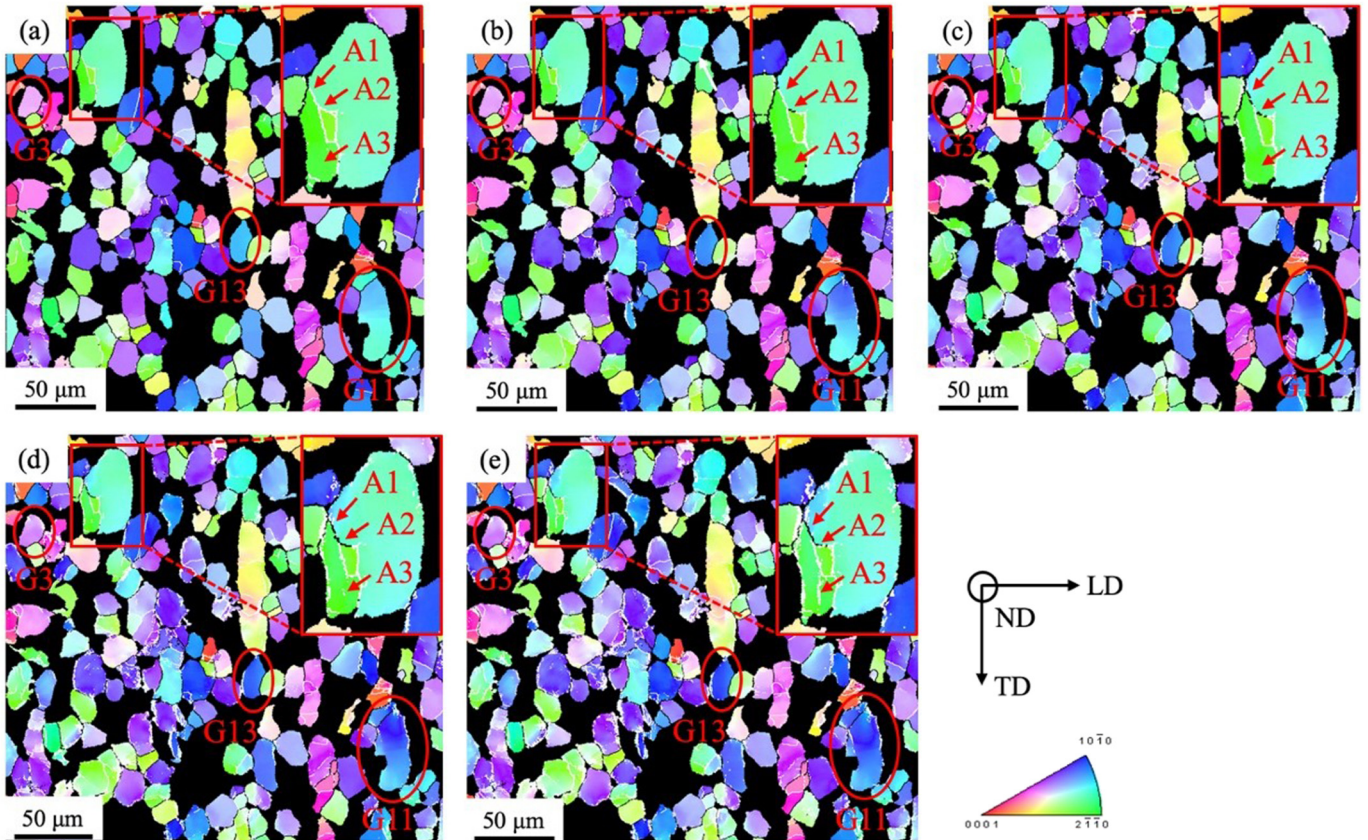


Fig. 4. Combinations of inverse pole figure maps and grain boundaries of α_p for the same area of a specimen with varying plastic strains: (a) 0%; (b) 1.2%; (c) 2.2%; (d) 3.6%; and (e) 4.9%. The colors correspond to α_p , and dark areas correspond to non- α_p , and black and white lines correspond to grain boundaries and sub-grain boundaries, respectively (ND: normal direction; TD: transverse direction; LD: loading direction). (For interpretation of the references to color in this figure legend, the reader is referred to the web version of this article.)

[28].

3.4. Activated slip system

Grain slip systems are activated to accommodate strain. It is well known that the formed slip line should be parallel to its slip plane. Based on theory, we constructed the plane trace analysis to confirm the specific activated slip system of each grain, as displayed in Fig. 6(a), which shows the IQ map of the same area as Fig. 4(b) at a plastic strain of 1.2%. The statistical slip systems are listed in Table 3. It can be seen that the prismatic slips are mainly (66.7%) activated during the strain. In Fig. 6(b), the typical slip lines, as a successively straight and regularly spaced morphology, exist in α_p .

The Schmid factor (SF) is an important parameter used to evaluate activated slip systems [11]. The SFs of typical 12-grains (i.e., G1–G12) and their sub-grains (Fig. 6(c)) are used to characterize activated slip systems during deformation. According to the results of the plane-trace analysis, the activated slip system of grains G1, G3, G6, and G12 are basal; the activated slip system of G2, G5, G8, G9, and G10 are prismatic; and the activated slip system of G4, G7, and G11 are 1st-order pyramidal. Table 4 lists the SFs of these grains. As shown, some grains, including G5, G9, and G10, are activated in the slip mode with a lower SF. Such phenomena can be explained by the effect of the critical resolved shear stress (CRSS) of the slip mode. The CRSS of the slip mode in the prism is lower than that activated in other slip modes [29]. Thus, the prismatic slip can much easier accumulate tensile residual lattice strains than can other activated slip modes. Similar behavior of the slip mode in Ti-6Al-4V was also characterized via theoretical simulation [30].

3.5. Grain rotation

In the previous section, the IPF maps (Fig. 4) having varying strains were used to characterize sub-grain boundaries. These IPF maps also can be used to observe grain rotation. As indexed by the red ellipse in Fig. 4, three typical grains (i.e., G3, G11, and G13) were used to analyze grain rotation. When the plastic strain reaches 1.2% (Fig. 4(b)), G3, G11, and G13 change in color, but with no transformation in morphology. This change implies a change in crystallographic orientation. In other words, it indicates that these two grains underwent rotation. When the specimen is strained to 2.2%, as in Fig. 4(c) and with previously named grains (i.e., G1–G12), nine out of 12 rotated. With an increase of strain in Fig. 4(d), most (i.e., 11 out of the selected 12) underwent rotation at varying degrees.

To further quantify the rotations of the selected 12 grains, the rotations were calculated using the Euler angles of each grain from the Bunge notation [31]. The relative rotation angle (θ) and axis pairs (r_1, r_2, r_3) of these 12 grains at different strains were calculated. These axis pairs were defined using the three axes of the 3-dimensional Cartesian coordinate system. Furthermore, the three axes should meet the conditions of $r_1^2 + r_2^2 + r_3^2 = 1$. Table 5 lists the relative rotation angles ($^\circ$) during deformation and the average rotation rate ($^\circ/\%$) after 6.2% plastic strain. As shown in Table 5, there are several rotation heterogeneities in these grains during straining. First, the rotation heterogeneity is detected within an individual grain after the same strain. For example, the rotation angle of G7 is 1.5° with a plastic strain varying from 3.6–4.9% (1.3% strain difference) and 2.1° with the plastic strain ranging from 4.9–6.2% (1.3% strain difference). Second, the rotation heterogeneity occurred among these grains activated in the same slip mode. For example, G1, G3, and G6 were all activated in basal.

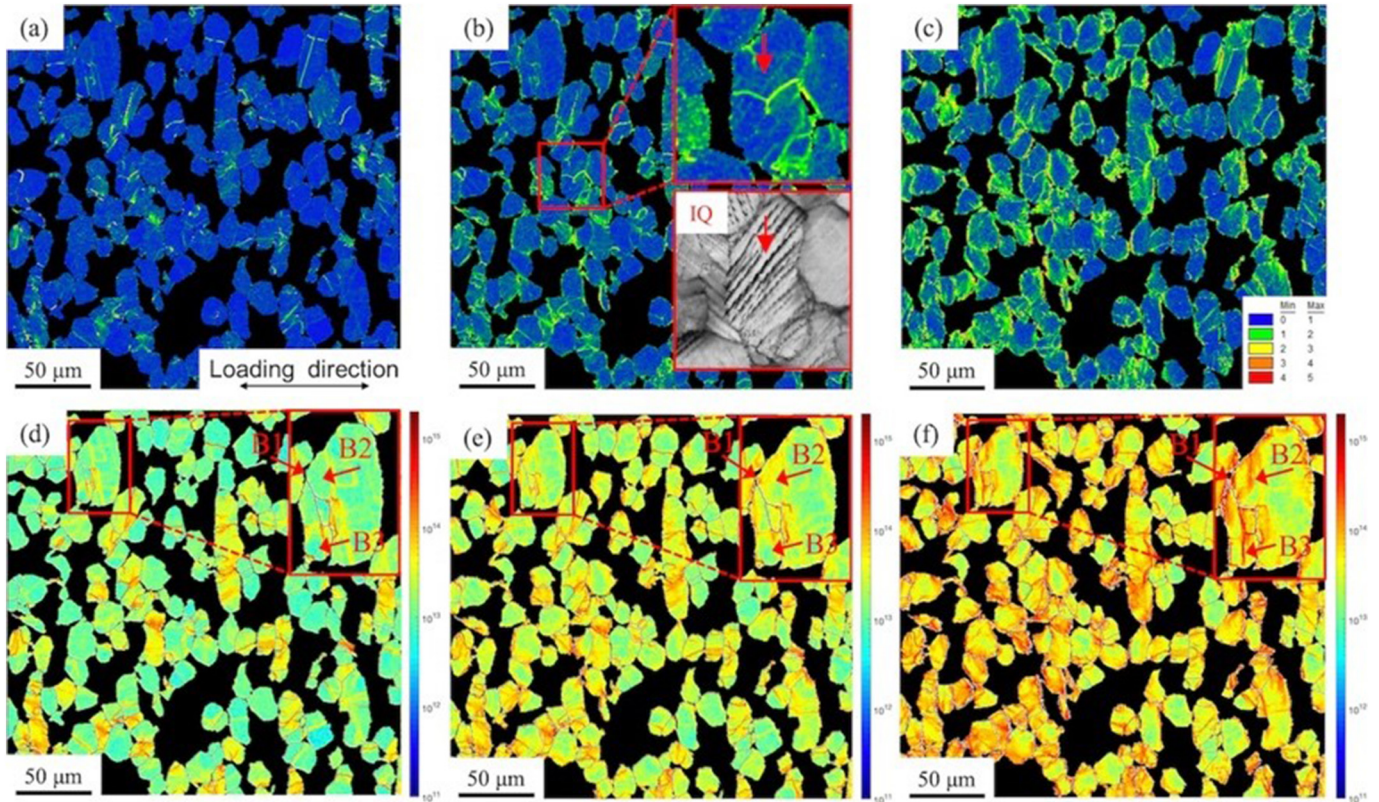


Fig. 5. Color-coded kernel average misorientation map of α_p with different plastic strains: (a) 0%; (b) 1.2%; (c) 4.9%; and the corresponding GND maps of the same area shown in (d) 0%; (e) 1.2%; and (f) 4.9%; respectively. (For interpretation of the references to color in this figure legend, the reader is referred to the web version of this article.)

However, their average rotation rates were $1.5^\circ/1$, $1.2^\circ/1$, and $2.1^\circ/1$, respectively. Such heterogeneity also occurred in grains activated in prism and the 1st-order pyramidal. Third, grains with different active slip modes showed rotation heterogeneity, including G1 (basal slip), G5 (prismatic slip), and G7 (1st-order pyramidal slip) with $1.5^\circ/1$, $2.1^\circ/1$, and $2.5^\circ/1$, respectively. Fourth, the grains having similar original orientation exhibited grain rotation heterogeneity, including G7 and G9, with an average rotation rate of $2.5^\circ/1$ and $0.8^\circ/1$, respectively. Such differences appeared in G2 and G10. Fifth, sub-grains of the grain showed different rotation rates, which could be found in the sub-grains of G2-1, G2-2, and G2-3. Such rotation heterogeneity was discovered in

Table 3

The result of the activated slip system in α_p after 1.2% plastic strain.

Slip system	Basal	Prismatic	1st-order pyramidal	2nd-order pyramidal	No slip
Grain numbers	17	68	10	0	7

other materials [14,15,18,20]. Via simulation calculation, Raabe et al. [19] showed that the effect of the initial orientation on grain rotation dominated deformation. Nevertheless, the magnitude of the effect was

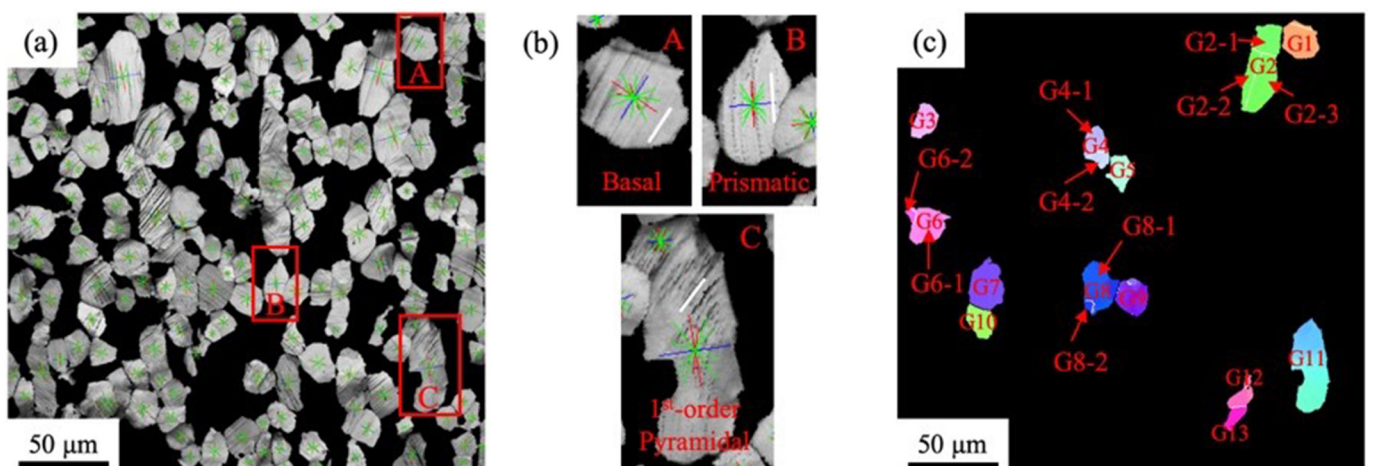


Fig. 6. (a) Image quality of α_p after 1.2% plastic deformation, blue line traced basal plane, red line traced prismatic plane, and green line traced 1st-order pyramidal plane; (b) amplified maps of selected areas in (a); and (c) IPF of the selected 12 grains and its sub-grains. (For interpretation of the references to color in this figure legend, the reader is referred to the web version of this article.)

Table 4
Schmid factors of selected 12 grains in different slip systems with no strain.

Grain	Sub-grain	Schmid factor in different slip system			
		Basal	Prismatic	1st-order pyramidal	2nd-order pyramidal
G1		0.47	0.17	0.30	0.36
G2	G2-1	0.24	0.44	0.45	0.49
	G2-2	0.23	0.43	0.44	0.49
	G2-3	0.24	0.43	0.45	0.49
G3		0.43	0.34	0.47	0.32
G4	G4-1	0.33	0.42	0.49	0.42
	G4-2	0.34	0.42	0.49	0.43
G5		0.29	0.45	0.49	0.47
G6	G6-1	0.46	0.28	0.43	0.23
	G6-2	0.45	0.25	0.42	0.23
G7		0.24	0.42	0.48	0.40
G8	G8-1	0.01	0.46	0.41	0.36
	G8-2	0.03	0.45	0.41	0.36
G9		0.24	0.40	0.47	0.38
G10		0.34	0.40	0.44	0.48
G11		0.12	0.48	0.49	0.44
G12	G12-1	0.45	0.19	0.35	0.33
	G12-2	0.42	0.16	0.34	0.34

different for each grain. Notably, the grain rotation in the orientation could be different under the same strain. This can be used to explain the rotation heterogeneity of grains in the studied material. Thus, the initial grain orientation should be responsible for the grain rotation heterogeneity.

3.6. Texture evolution

Fig. 7 shows the IPFs of α_p under straining, in which the observed direction is parallel to the loading direction. The original texture already exhibits maxima near $\langle 10\bar{1}1 \rangle$ and secondary maxima near $\langle 10\bar{1}0 \rangle$ and $\langle 2\bar{1}\bar{1}1 \rangle$, related to the original thermomechanical processes of the material. During deformation, there are four significant characteristics in the texture: (i) the $\langle 2\bar{1}\bar{1}1 \rangle$ texture is rotated gradually to the $\langle 10\bar{1}1 \rangle$ texture; (ii) the $\langle 10\bar{1}1 \rangle$ texture becomes increasingly stronger (evidenced by the maximum of texture intensity) and rotated slowly to

$\langle 10\bar{1}0 \rangle$ texture at the same time; (iii) the $\langle 10\bar{1}0 \rangle$ texture becomes stronger step-by-step; and (iv) the $\langle 0001 \rangle$ and $\langle 2\bar{1}\bar{1}0 \rangle$ textures were stable.

4. Discussion

4.1. Grain rotation path

As mentioned, the slip system, rotation angle, and average rotation rate of the selected 12 grains (Fig. 6(c)) were analyzed. The rotation path of these grains was needed for further study. Fig. 8 shows the IPF maps of tensile directions of the 12 grains with varying strains. The rotation path of each grain is arrowed in black. As displayed in G2, the rotation path of the sub-grains within the individual grain is a bit different, possibly owing to the increased misorientations among these sub-grains under deformation. Although G1, G3, and G6 were all activated in basal mode, their rotation paths were quite different. For the G10, it almost had no rotation trace. The rotation paths of some grains (e.g., G1, G5, and G12) were straight. However, the rotation paths of others (e.g., G2, G4, and G6) were no longer straight. As seen from the differentiated rotation paths, the rotation paths of these grains in the loading direction were strongly dependent on the original orientations of each grain.

In light of the characteristics of grain rotation, the rotation paths of the selected 12 grains can be classified into two types: A and B. This is displayed in Fig. 9. Type A indicates that the grains were rotated to the straight line connecting the $\langle 0001 \rangle$ pole with the $\langle 2\bar{1}\bar{1}0 \rangle$ pole and then were moved to the straight line connecting the $\langle 0001 \rangle$ pole with the $\langle 10\bar{1}0 \rangle$ pole. It finally proceeded to the $\langle 10\bar{1}1 \rangle$ pole, as shown in G1, G3, G6, and G12. As described in the previous section, all the grains of type A were activated in basal. For type B, the rotation paths moved to the straight line connecting the $\langle 0001 \rangle$ pole with the $\langle 10\bar{1}0 \rangle$ pole. It finally rotated to the $\langle 10\bar{1}0 \rangle$ pole. Grains belonging to type B were G2, G4, G5, G7, G8, and G11, activated in prismatic or 1st-order pyramidal. Moreover, G9, being activated in prismatic with double slip modes, showed the opposite direction in the rotation path (marked by the red ellipse in Fig. 9) comparing the two types (A and B).

The different rotation axes explain the differentiated rotation paths. The Taylor axis is the grain rotation axis and is proposed based on the

Table 5
Calculated rotation angles and average rotation rates for the selected 12 grains.

Grain	Sub-grain	Rotation degree (°)					Average rotation rate (°/1%)	Slip system
		From $\varepsilon = 0\%$ to $\varepsilon = 1.2\%$	From $\varepsilon = 1.2\%$ to $\varepsilon = 2.2\%$	From $\varepsilon = 2.2\%$ to $\varepsilon = 3.6\%$	From $\varepsilon = 3.6\%$ to $\varepsilon = 4.9\%$	From $\varepsilon = 4.9\%$ to $\varepsilon = 6.2\%$		
G1		3.6	1.0	0.7	1.2	2.9	1.5	Basal
G2	G2-1	1.2	3.1	6.6	0.5	3.8	2.5	Prism
	G2-2	2.1	2.9	3.4	1.6	1.9	1.9	Prism
	G2-3	2.5	2.9	4.7	1.0	2.5	2.0	Prism
G3		0.7	2.7	1.4	2.0	0.9	1.2	Basal
G4	G4-1	2.9	3.1	5.2	1.5	3.4	2.6	1st-order pyramidal
	G4-2	3.3	2.1	4.2	0.9	3.1	2.2	1st-order pyramidal
G5		2.3	3.3	3.9	1.0	2.5	2.1	Prism
G6	G6-1	1.9	5.8	1.5	3.3	0.5	2.1	Basal
	G6-2	1.1	4.3	1.8	3.7	1.2	2.1	Basal
G7		3.3	3.8	5.0	1.5	2.1	2.5	1st-order pyramidal
G8	G8-1	2.1	1.2	1.0	0.5	0.1	0.8	Prism
	G8-2	0.6	2.0	2.0	0.3	0.6	0.8	Prism
G9		1.2	1.6	1.2	0.6	0.5	0.8	Prism
G10		0.9	1.7	0.8	1.6	0.3	0.9	Prism
G11		0.8	4.1	3.8	2.7	1.6	2.1	1st-order pyramidal
G12	G12-1	0.6	2.5	1.3	2.0	0.7	1.1	Basal
	G12-2	0.5	2.8	1.3	2.0	0.4	1.1	Basal

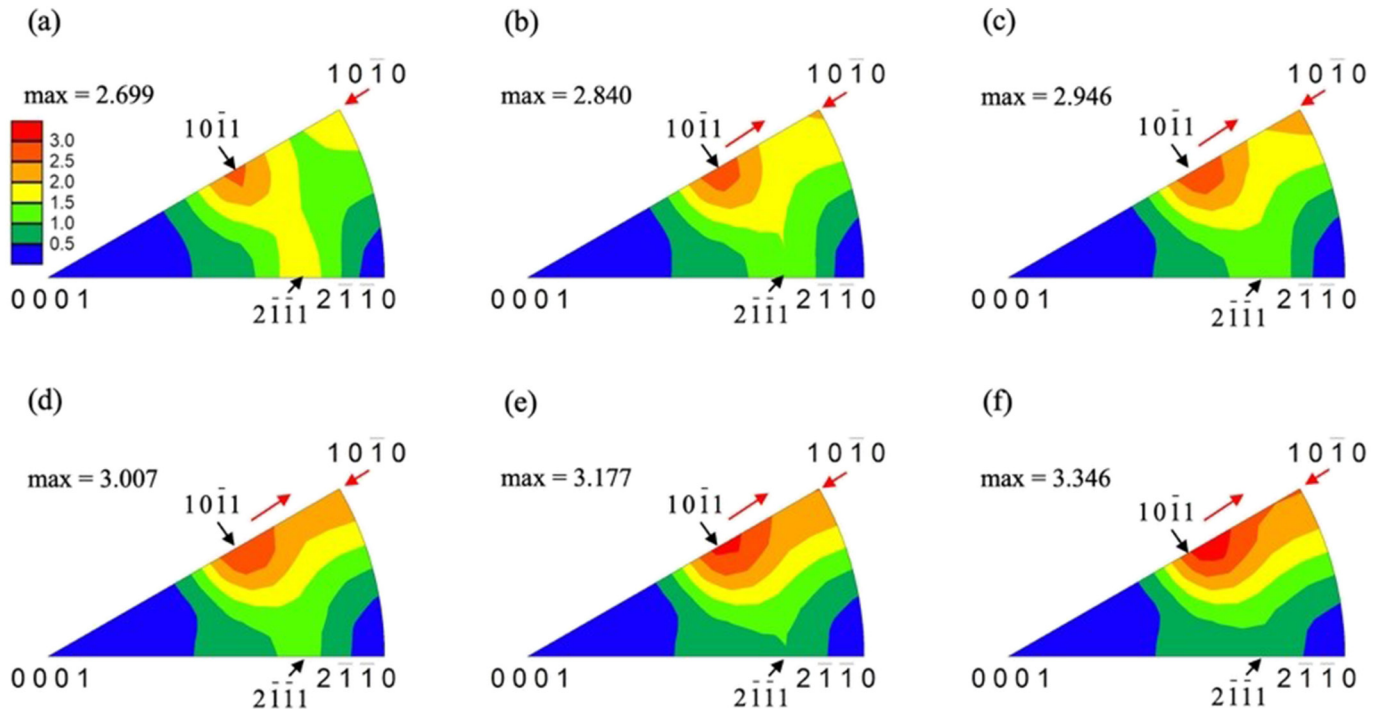


Fig. 7. IPFs for α_p in the loading direction with different plastic strains: (a) 0%; (b) 1.2%; (c) 2.2%; (d) 3.6%; (e) 4.9%; and (f) 6.2%.

slip plane normal and slip direction. It is applied to characterize the deformation modes of α -Ti and α -Zr [32]. Table 6 lists the deformation slip systems and corresponding Taylor axes [32–34]. As shown in Table 6, the basal slip mode has three variants of the Taylor axis, which result in the differentiated rotation paths of these grains (e.g., G1, G3, and G6). Such a phenomenon occurred in grains activated in the prismatic and 1st-order pyramidal slips, because of the different Taylor axes and selected variants. However, the rotation paths of G9 showed the opposite direction compared with types A and B, and could not comply with the Taylor axes. This could be because of the appearance of double slip modes in G9, which are not suitable for the Taylor axis [32].

4.2. The relationship of grain rotation path with texture evolution

According to [18], the grain rotation path has a relationship with the texture evolution in the polycrystalline aluminum alloy. This can also happen with Ti-6Al-4V. Comparing Fig. 9 with the texture maps of Fig. 7, it can be seen that, as the strain increases, rotation paths of type A (grains activated in basal slip) gradually move to the $\langle 10\bar{1}1 \rangle$ pole, and increase the intensity of the $\langle 10\bar{1}1 \rangle$ texture. Meanwhile, rotation paths of type B (grains activated in prismatic or 1st-order pyramidal slip) move to the $\langle 10\bar{1}0 \rangle$ pole and enhance the intensity of the $\langle 10\bar{1}0 \rangle$ texture. We can thus conclude that the rotation behavior of the selected 12 grains are consistent with the texture evolution of all α_p grains. Such consistency provides a reference for further study of the texture evolution of Ti alloys.

4.3. Effect of grain rotation and texture evolution on mechanical properties

As shown in Table 2, the measured tensile strength by the in situ tensile tests was higher than those measured by the regular tensile test. The difference may be related to the texture evolution and work hardening. According to the Hall-Petch equation [35], the flow stress of a material can be expressed as: $\sigma(\epsilon) = \sigma_0(\epsilon) + \kappa(\epsilon)d^{-0.5}$, in which $\sigma_0(\epsilon)$ and $\kappa(\epsilon)$ are constants at a specific strain, d is the grain size in mm and $\sigma(\epsilon)$ is the flow stress at a specific strain [14]. Yegneswaran et al. [36]

stated that texture could influence the slip within a polycrystal, which in turn affects the $\kappa(\epsilon)$ value. E. Cerreta et al. [37] found in high purity hafnium that the $\sigma_0(\epsilon)$ and $\kappa(\epsilon)$ increased with the increasing strain at room temperature, due to the dislocation pile-ups at grain boundaries. The situation can be applied to the studied material. From the GND maps (Fig. 5(d)–(f)), the dislocation tangle or wall formed under the deformation leading to the formation of sub-grain boundaries. A parent grain fragmented into several sub-grains. These formed sub-grain boundaries, in turn, blocked the dislocation glide, which contributed to the dislocation tangle further and caused the work hardening during the plastic strain, leading to a higher tensile strength of the in situ tensile tests.

Hirsch et al. [38] reported that any variation in crystallographic texture would have an immediate impact on the strength of material owing to the changes in the geometry of the different slip modes activated upon ongoing or subsequent deformation. As previously discussed, the grain rotation path is consistent with the texture evolution. The $\langle 10\bar{1}1 \rangle$ texture and $\langle 10\bar{1}0 \rangle$ texture was enhanced. With the texture evolution during the strain, the grain rotated, and well-aligned along the loading direction, as well as grain size, decreased. Such enhanced texture maybe reduce ductility in a particular direction and increase mechanical anisotropy [38].

5. Conclusions

The in situ tensile test and EBSD technique were performed to study the deformation behavior and active slip systems of grain boundaries, dislocations, textures, and grain rotations of α_p in Ti-6Al-4V. The main conclusions are drawn as follows:

- (1) During the in situ tensile test, the activation of multiple slip systems and grain rotations both occurred in response to deformation. Most (66.7%) of the α_p grain were activated in prismatic slip systems obtained from plane-trace analysis.
- (2) From the KAM and GNDs analyses, the dislocations mainly distributed near grain and sub-grain boundaries, and partially distributed around slip lines. Under straining, the slip line formed in

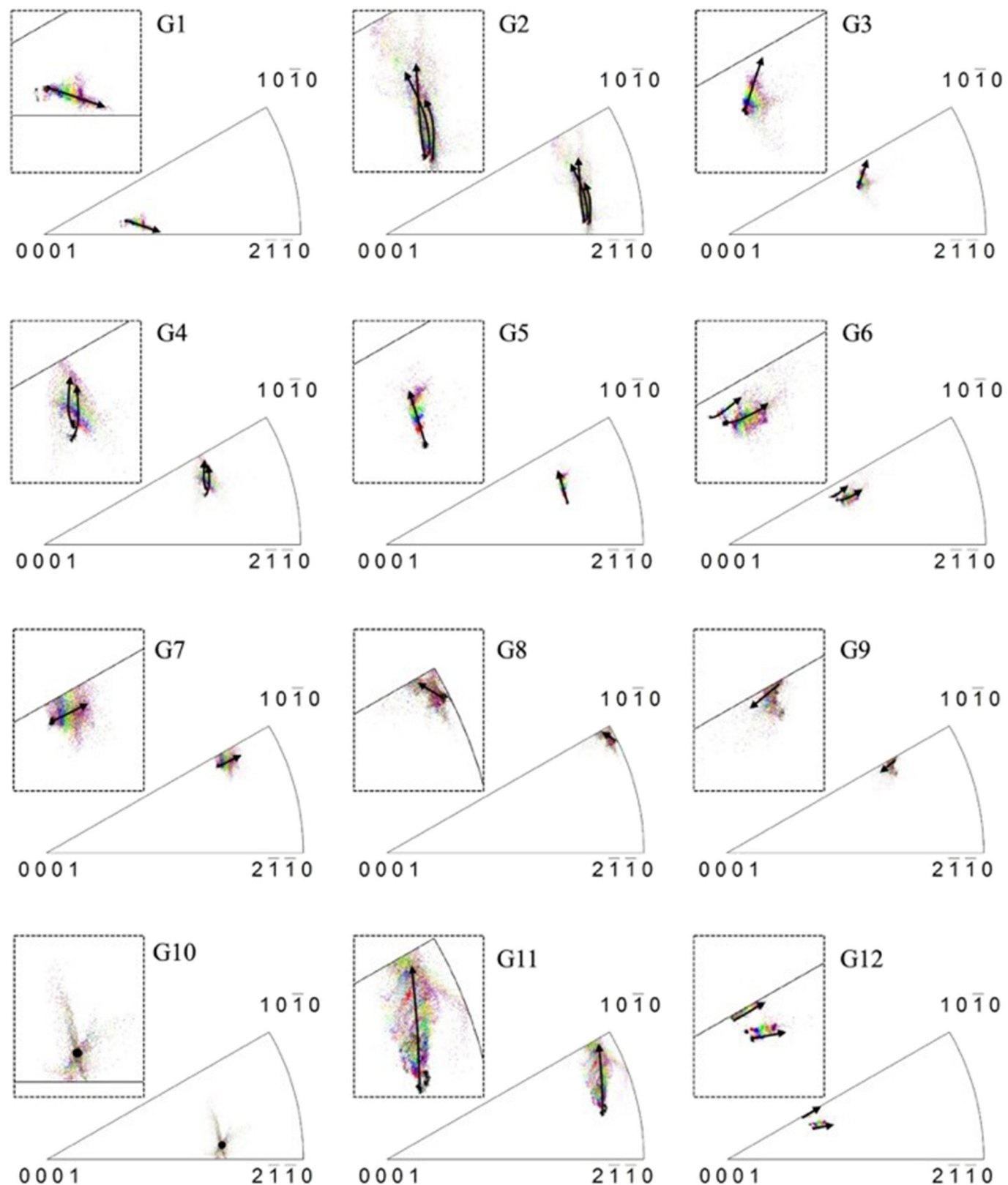


Fig. 8. IPF maps of the tensile directions of 12 grains at different plastic strains shown in different colors: 0%, 1.2%, 2.2%, 3.6%, 4.9%, and 6.2% correspond to black, red, blue, green, yellow, and purple, respectively. (For interpretation of the references to color in this figure legend, the reader is referred to the web version of this article.)

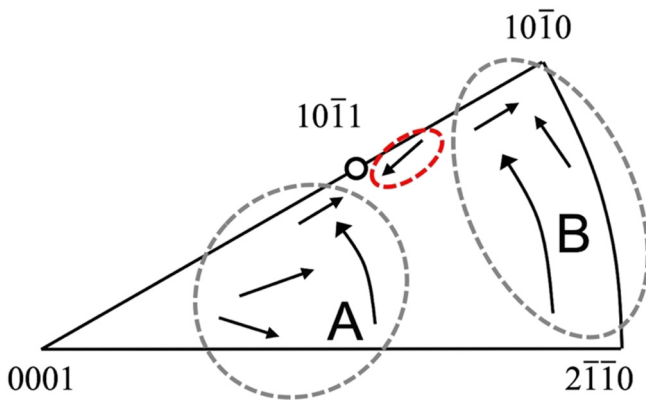


Fig. 9. Schematic for the rotation paths of the tensile direction of the selected 12 grains.

Table 6
Deformation modes of α -Ti and α -Zr and corresponding Taylor axes [32–34].

Deformation mode	Total number of slip variants	Taylor axis	Total number of variants of the Taylor axis
{01-10} <2110>	3	<0001>	1
{0002} <2110>	3	<01-10>	3
{01-11} <2110>	6	<0112>	6
{01-11} <1-123>	12	<13853>	12
{12-11} <1-123>	12	<61-53>	12
{01-11} <1-123>	6	<1100>	3

grains, and the dislocation activities led to the formation of LAGBs and its transformation to HAGBs.

- (3) The rotation heterogeneity of the tensile direction of α_p was found via the analysis of rotation angles, average rotation rates, and rotation paths.
- (4) As observed from the loading direction, grain rotation paths kept up with the texture evolution directions of all α_p . During deformation, rotation paths of grains activated in the basal slip gradually moved toward the <10-11> pole, which increased the intensity of the <10-11> texture. Meanwhile, rotation paths of other grains activated in prismatic or 1st-order pyramidal slips moved to the <10-10> pole, which enhanced the intensity of the <10-10> texture. Grain rotation and texture evolution are correlated with mechanical properties.

Data availability

The raw data required to reproduce these findings cannot be shared at this time as the data also form part of an ongoing study. The processed data required to reproduce these findings are available from the corresponding author upon request.

Declaration of competing interest

The authors declare that they have no known competing financial interests or personal relationships that could have appeared to influence the work reported in this paper.

Acknowledgements

This research was supported by the Cross-Ministerial Strategic Innovation Promotion Program (SIP) from the Cabinet Office, Government of Japan.

References

- [1] T. Zhu, M. Li, Lattice variations of Ti-6Al-4V alloy with hydrogen content, Mater. Charact. 62 (2011) 724–729.
- [2] C.C. Shen, C.M. Wang, Effects of hydrogen loading and type of titanium hydride on grain refinement and mechanical properties of Ti-6Al-4V, J. Alloys Compd. 601 (2014) 274–279.
- [3] S. Hémery, P. Villevieille, On the influence of ageing on the onset of plastic slip in Ti-6Al-4V at room temperature: insight on dwell fatigue behavior, Scr. Mater. 130 (2017) 157–160.
- [4] Q. Wang, Z. Liu, Plastic deformation induced nano-scale twins in Ti-6Al-4V machined surface with high speed machining, Mater. Sci. Eng. A 675 (2016) 271–279.
- [5] B. Barkia, J.P. Couzinié, S. Lartigue-Korinek, I. Guillot, V. Doquet, In situ TEM observations of dislocation dynamics in α titanium: effect of the oxygen content, Mater. Sci. Eng. A 703 (2017) 331–339.
- [6] P. Castany, F. Pettinari-Sturmel, J. Douin, A. Coujou, TEM quantitative characterization of short-range order and its effects on the deformation micromechanisms in a Ti-6Al-4V alloy, Mater. Sci. Eng. A 680 (2017) 85–91.
- [7] Y.G. Liu, M.Q. Li, Stress-induced twinning of nanocrystalline hexagonal close-packed titanium in Ti-6Al-4V, Mater. Lett. 180 (2016) 47–50.
- [8] Y.G. Liu, M.Q. Li, H.J. Liu, Deformation induced face-centered cubic titanium and its twinning behavior in Ti-6Al-4V, Scr. Mater. 119 (2016) 5–8.
- [9] C. Tan, Q. Sun, L. Xiao, Y. Zhao, J. Sun, Slip transmission behavior across α/β interface and strength prediction with a modified rule of mixtures in TC21 titanium alloy, J. Alloys Compd. 724 (2017) 112–120.
- [10] Z. Zheng, S. Waheed, D.S. Balint, F.P.E. Dunne, Slip transfer across phase boundaries in dual phase titanium alloys and the effect on strain rate sensitivity, Int. J. Plast. 104 (2018) 23–38.
- [11] S. Zhang, W. Zeng, Q. Zhao, L. Ge, M. Zhang, In situ SEM study of tensile deformation of a near- β titanium alloy, Mater. Sci. Eng. A 708 (2017) 574–581.
- [12] Q. Wang, Z. Liu, B. Wang, A.U. Hassan Mohsan, Stress-induced orientation relationship variation for phase transformation of α -Ti to β -Ti during high speed machining Ti-6Al-4V, Mater. Sci. Eng. A 690 (2017) 32–36.
- [13] S. Waheed, Z. Zheng, D.S. Balint, F.P.E. Dunne, Microstructural effects on strain rate and dwell sensitivity in dual-phase titanium alloys, Acta Mater. 162 (2019) 136–148.
- [14] W.S. Li, H.Y. Gao, H. Nakashima, S. Hata, W.H. Tian, In-situ study of the deformation-induced rotation and transformation of retained austenite in a low-carbon steel treated by the quenching and partitioning process, Mater. Sci. Eng. A 649 (2016) 417–425.
- [15] G.K. Tirumalasetty, M.A. Van Huis, C. Kwakernaak, J. Sietsma, W.G. Sloof, H.W. Zandbergen, Deformation-induced austenite grain rotation and transformation in TRIP-assisted steel, Acta Mater. 60 (2012) 1311–1321.
- [16] H.D. Joo, J.S. Kim, K.H. Kim, N. Tamura, Y.M. Koo, In situ synchrotron X-ray microdiffraction study of deformation behavior in polycrystalline coppers during uniaxial deformations, Scr. Mater. 51 (2004) 1183–1186.
- [17] L. Margulies, G. Winther, H.F. Poulsen, In situ measurement of grain rotation during deformation of polycrystals, Science (80-) 291 (2001) 2392–2394.
- [18] J.H. Han, K.K. Jee, K.H. Oh, Orientation rotation behavior during in situ tensile deformation of polycrystalline 1050 aluminum alloy, Int. J. Mech. Sci. 45 (2003) 1613–1623.
- [19] D. Raabe, Z. Zhao, W. Mao, On the dependence of in-grain subdivision and deformation texture of aluminum on grain interaction, Acta Mater. 50 (2002) 4379–4394.
- [20] P. Chen, S.C. Mao, Y. Liu, F. Wang, Y.F. Zhang, Z. Zhang, X.D. Han, In-situ EBSD study of the active slip systems and lattice rotation behavior of surface grains in aluminum alloy during tensile deformation, Mater. Sci. Eng. A 580 (2013) 114–124.
- [21] A.K. Saxena, A. Tewari, P. Pant, Quantitative analysis of orientation and near neighbor interaction effects during deformation of polycrystalline Ti6Al4V, Mater. Sci. Eng. A 648 (2015) 1–8.
- [22] I.G. Dastidar, V. Khademi, T.R. Bieler, A.L. Pilchak, M.A. Crimp, C.J. Boehlert, The tensile and tensile-creep deformation behavior of Ti-8Al-1Mo-1V (wt%), Mater. Sci. Eng. A 636 (2015) 289–300.
- [23] M. Calcagnotto, D. Ponge, E. Demir, D. Raabe, Orientation gradients and geometrically necessary dislocations in ultrafine grained dual-phase steels studied by 2D and 3D EBSD, Mater. Sci. Eng. A 527 (2010) 2738–2746.
- [24] A. Kundu, D.P. Field, Influence of plastic deformation heterogeneity on development of geometrically necessary dislocation density in dual phase steel, Mater. Sci. Eng. A 667 (2016) 435–443.
- [25] J. Jiang, T.B. Britton, A.J. Wilkinson, Evolution of dislocation density distributions in copper during tensile deformation, Acta Mater. 61 (2013) 7227–7239.
- [26] Y. Liu, M. Li, Nanocrystallization mechanism of beta phase in Ti-6Al-4V subjected to severe plastic deformation, Mater. Sci. Eng. A 669 (2016) 7–13.
- [27] X.D. Ren, W.F. Zhou, F.F. Liu, Y.P. Ren, S.Q. Yuan, N.F. Ren, S.D. Xu, T. Yang, Microstructure evolution and grain refinement of Ti-6Al-4V alloy by laser shock processing, Appl. Surf. Sci. 363 (2016) 44–49.
- [28] J.L. Sun, P.W. Trimby, F.K. Yan, X.Z. Liao, N.R. Tao, J.T. Wang, Shear banding in commercial pure titanium deformed by dynamic compression, Acta Mater. 79 (2014) 47–58.
- [29] H. Li, D.E. Mason, T.R. Bieler, C.J. Boehlert, M.A. Crimp, Methodology for estimating the critical resolved shear stress ratios of α -phase Ti using EBSD-based trace analysis, Acta Mater. 61 (2013) 7555–7567.
- [30] A.M. Stapleton, S.L. Raghunathan, I. Bantounas, H.J. Stone, T.C. Lindley, D. Dye, Evolution of lattice strain in Ti-6Al-4V during tensile loading at room temperature, Acta Mater. 56 (2008) 6186–6196.

- [31] V. Randle, O. Engler, Introduction to Texture Analysis: Macrotexture, Microtexture and Orientation Mapping, (2014).
- [32] Y.B. Chun, M. Battaini, C.H.J. Davies, S.K. Hwang, Distribution characteristics of in-grain misorientation axes in cold-rolled commercially pure titanium and their correlation with active slip modes, *Metall. Mater. Trans. A Phys. Metall. Mater. Sci.* 41 (2010) 3473–3487.
- [33] E.J. Rappoport, C.A. Hartley, Deformation Modes of Zirconium at 77, 575, and 1075 K, United States, (1960).
- [34] A.T. Churchman, The slip modes of titanium and the effect of purity on their occurrence during tensile deformation of single crystals, *Proc. R. Soc. A Math. Phys. Eng. Sci.* 226 (1954) 216–226.
- [35] N. Hansen, B. Ralph, The strain and grain size dependence of the flow stress of copper, *Acta Metall.* 30 (1982) 411–417.
- [36] A.H. Yegneswaran, K.S. Raman, Y. Gada, V.R.K. Proasad, Texture and grain size dependence of tensile properties in warm rolled cadmium, *Zeitschrift Fuer Met. Res. Adv. Tech.* 71 (1980) 253–259.
- [37] E. Cerreta, C.A. Yablinsky, G.T. Gray, S.C. Vogel, D.W. Brown, The influence of grain size and texture on the mechanical response of high purity hafnium, *Mater. Sci. Eng. A* 456 (2007) 243–251.
- [38] J. Hirsch, T. Al-Samman, Superior light metals by texture engineering: optimized aluminum and magnesium alloys for automotive applications, *Acta Mater.* 61 (2013) 818–843.